# Development of Computer-Vision-Based Technique for Prestress Measurement in Beams

B. Yaswanth Sandeep[ID] and C. Chandraprakash[ID]

*Abstract*— **We report the first work on demonstrating the measurement of prestresses in beams using methods of computer vision (CV). Toward this, we developed instruments, performed experiments, and implemented image processing algorithms. First, custom-made equipment were designed and developed to achieve fixed-free, fixed-fixed, fixed-pinned, and pinned-pinned boundary conditions and prestress. Beams of steel, aluminum, copper, and glass fiber epoxy composite (GFEC) were constrained to these four types of boundary conditions. The vibrations of the beams in static tensile axial loads were recorded using a smartphone camera via a lock-in mechanism. A total of 320 experiments involving all boundary conditions and ten axial loads were performed. Resonant frequencies were identified from the videos using image correlation and point-tracking algorithms. Young's moduli were estimated from experiments with no axial load. Prestresses were determined from the resonant frequencies and were found to have excellent correlations with experimental values. This method can be easily extended to identify the prestress in beams with lateral loads and to 3-D objects.**

*Index Terms*— **Beams, computer vision (CV), image correlation algorithms, natural frequency, prestress.**

## I. INTRODUCTION

**B**EAMS have been the classical elements in structural mechanics, leading to applications from bridges to microelectromechanical systems to interconnects in electronics. The main purpose of a beam is to sustain loads applied laterally to the beam's axis. Stress is the resistance to the application of loads such as forces, displacement, torsion, or twisting on objects. The interest of a design engineer is to ensure the stresses developed in the structures, including beams, lie well within the yield limit of the material. Engineered structures are made of one or more components, each of which is subjected to a sequence of casting or molding, machining, and assembling operations [1] or installation [2]. Stresses develop in the material due to these operations. As it is impractical to subject the components or the structure to annealing after every operation, these stresses remain in the structure, and hence are referred to as residual stresses or prestresses.

Residual stress or prestress in a structure can lead to local elastic or plastic deformation. The presence of residual or prestress stress also influences the life cycle of a component [3]. Compressive prestresses enhance the life of the structure, whereas tensile stresses often decrease the effective load-bearing capacity of the structure leading to failure. Such failures due to prestresses are reported in batteries [4], beams [5], bridges [6], etc. Furthermore, prestress can also alter the phase speeds of the elastic waves in homogeneous [7], [8] and inhomogeneous structures such as phononic crystals [9]. Thus, the determination of residual stress and prestress is not only useful to understand and predict the remaining useful life of a component but also to correct the methods using elastic waves.

In this work, we focus on the estimation of prestress. As residual stresses and prestresses are not a result of controlled loads, these are difficult to estimate or measure directly using strain gauges and constitutive relations [10], photoelastic methods [11], ultrasonic nondestructive methods [12], thermoelastic stress analysis, etc. To date, methods to estimate prestress have been done using strain gauges [10], X-rays [13], fiber Bragg gratings, ultrasonic non-destructive evaluation (NDE) [7], [14], etc. Most of these methods use contact-based sensors, and the existing noncontact-based methods using X-rays or neutrons are unsuitable for periodic field inspections. Methods to continuously measure and monitor prestress were also developed by preinstalled piezoelectric sensors [15]. As the aforementioned methods do not work for larger and immovable structures in service, a need exists for robust, noncontact, alternative prestress measurement systems. A nonzero value of prestress alters the phase velocity of elastic waves—called acoustoelastic effect [16]—and the natural frequency of the structure. Based on the acoustoelastic effect, in 2020, an ultrasonic nondestructive technique was developed to monitor the variation in prestress with time [17]. Despite these recent advances, the following challenges exist.

1) *Accessibility:* In many cases, it can be difficult to access the required location, making it challenging to install sensors.
2) *Structural Health Monitoring:* Sensors have to be installed in the beams during fabrication, must be locally powered, and should be connected to the network for data acquisition; all these make it economically expensive.
3) *Ease, Cost, and Portability:* Techniques involving X-rays have specialized bulky expensive equipment. Likewise, ultrasonic equipment is also expensive and require specialized skills to operate.

While traditional methods to measure stresses or strains use contact-type sensors, noncontact methods using images and

lasers have gained attention for the measurement of properties. The use of computer and images for the reconstruction of a scene has led to the development of computer vision (CV). Methods of CV have been used to inspect traditional and additively [18] manufactured products to assess the quality, detect cracks in concrete [19], estimate planar angles from nonorthogonal imaging [20], increase tool life [21], inspect pharmaceuticals [22], detect defects in flat steel surfaces [23], reconstruction of millimeter-sized droplets [24], etc. Many of the experiments were performed with a smartphone. Full-field measurements of flow or displacement, which are otherwise tedious or impossible, can be made in seconds using methods of CV.

Advancements were also made to determine the material properties of vibrating objects using high-speed video cameras. These methods are categorized as visual vibrometry. In the first work [25], methods to determine the material properties of beams and fabrics, vibrating due to acoustic white noise or air currents, were established using high-speed cameras. Methods also exist to extract the displacement fields or frequency spectrum from video. Local motions of the objects from the video were extracted using the complex steerable pyramid (CSP) [26], [27] to construct the frequency spectrum and determine the dominant mode. From this, natural frequencies were identified and correlated with material properties. Thus, high-speed cameras were demonstrated to be capable as visual microphones [28]. The in-plane motion and velocities can be extracted using the optical flow method [29]. As is well-known, the digital image correlation (DIC) is also a good option to get a deformation field [30]. CV-based methods can address some challenges of the traditional measurement methods.

1) *Noncontact Method:* The analysis in many methods of CV and visual vibrometry requires only a noncontact mode of the trigger to the specimen. This makes the method a nondestructive technique.

2) *Speed and Efficiency:* Traditional equipment, including simple strain gauges, require more skill, larger times to set up (in minutes), and analysis. In contrast, CV-based methods take less setup time (in minutes), take a less-skilled person to perform experiments, and have faster processing times (in seconds).

3) *Cost-Effectiveness:* CV-based methods require a camera. As smartphones are ubiquitous with an embedded camera, this essentially minimizes the cost of the equipment, when compared with conventional methods for prestress prediction.

4) *Accessibility:* As smartphones are widely used, and our method depends on the embedded camera, this method is easily implementable. Equipment for X-ray and magnetostrictive methods may be specialized and not as readily available for use in a field or shop floor.

To the best of our knowledge, there are no specific methods reported in the literature that calculate stress directly using methods of machine vision. In a project dedicated to the investigation of failure in structures due to prestress, here we undertook a fundamental study to quantify the prestress using noncontact methods in basic structures, made of different

TABLE I
DETAILS OF SPECIMENS. GFEC STANDS FOR GLASS FIBER EPOXY COMPOSITE. DENSITIES WERE CALCULATED

| Specimen ID | Material | Thickness (mm) | Width (mm) | Density (kg/m$^3$) |
|---|---|---|---|---|
| 1 | Aluminum | 1.96 | 24.98 | 2633.1 |
| 2 | Aluminum | 1.96 | 10.50 | 2633.1 |
| 3 | Stainless steel | 3.09 | 12.60 | 7625.6 |
| 4 | Stainless steel | 1.50 | 9.10 | 7375.1 |
| 5 | Copper | 3.00 | 12.00 | 8588.2 |
| 6 | Copper | 1.78 | 6.61 | 8410.2 |
| 7 | GFEC | 2.63 | 13.80 | 1604.9 |
| 8 | GFEC | 2.63 | 9.74 | 1604.9 |

materials, subjected to various boundary conditions. We developed a CV-based method to determine prestress in beams based on changes in natural frequencies—a method that fits in visual vibrometry. We prepared beams of commonly available metals and polymers of varying lengths and subjected them to fixed-free, fixed-fixed, fixed-pinned, or pinned-pinned conditions. These beams were statically loaded along their axes. Impact loads were given to the beams, and the full-field displacements of the vibrating beams were recorded by an optical camera of a smartphone. The vibrations were analyzed by an algorithm similar to DIC [30] using "sum of absolute difference" (SAD) as a correlation measure and the natural frequencies were identified. The natural frequencies were compared with the theoretical predictions and the values of prestresses (due to the axial loads) were estimated. Our method is similar to how DIC correlates frames to each other. We chose this method because of its simplicity and less computational cost. The innovation of this work is the integration of a newly developed simple experimental setup with the existing computer programs and theory to predict prestresses, which are otherwise difficult to measure.

The plan for the rest of this article is as follows. In Section II, we describe the construction of the equipment and the detailed experimental procedure. The extraction of displacement from image processing is described in Section III. The theoretical basis is presented in Section IV. The results of all the experiments, and comparisons with theory, are presented and discussed in Section V. We end with key conclusions in Section VI.

## II. EXPERIMENTS: MATERIALS AND METHODS

### A. Materials

We performed experiments with specimens made of four different materials, two different cross-sections in each material, and four different pairs of boundary conditions. The lengths of specimens vary with the experiment. The thicknesses and widths of all the specimens were measured with a digital vernier caliper (Mitutoyo, Japan). Measuring the lengths and weights of beams, the densities were calculated. The specimens used and basic measurements are tabulated in Table I. All the fixtures and pins used in these experiments are made of mild steel. A nylon rope running over a pulley was used to apply axial load. All the bearings used are made of stainless steel. A fast-setting adhesive based on cyanoacrylate (Fevikwik) was used wherever necessary.
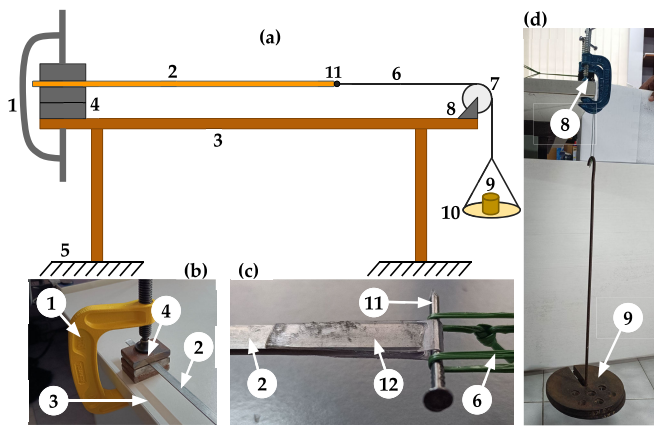
Fig. 1. Fixed-free boundary condition implementation. 1—Clamp. 2—Beam. 3—Table. 4—Metal blocks. 5—Ground. 6—Cable. 7—Pulley. 8—Pulley fixture. 9—Weights. 10—Pan. 11—Pin attached to beam. 12—Plastic sheet attached to beam. (a) Schematic of the setup. Photographs of (b) fixed and (c) free boundary conditions, and (d) weights hung from axial-load-applying cable.

### B. Construction of the Experimental Setups

Four different setups were prepared each corresponding to one of the four different pairs boundary conditions: 1) fixed-free; 2) fixed-fixed; 3) fixed-pinned; and 4) pinned-pinned. Different mechanisms were implemented to achieve all types of boundary conditions.

*1) Beam in Fixed-Free Condition:* The schematic for this is shown in Fig. 1(a). The fixed boundary condition requires the deflection and slope of the beam to be zero. This was achieved by sandwiching the beam between two flat mild steel blocks and clamping them to a table using a C-clamp. This arrangement is shown in Fig. 1(b). The free boundary condition requires no restriction on the movement at that end and yet axial load had to be applied to the beam. To achieve this condition, a plastic sheet was attached using adhesive to each specimen, such that a pin can be attached as shown in Fig. 1(c). The pin was laterally stressed by a string that is attached to the load-applying cable, as shown in Fig. 1(d).

*2) Beam in Fixed-Fixed Condition:* The schematic of the setup is shown in Fig. 2(a). The fixed-fixed boundary conditions require the displacement and slope of the beam to be zero at both ends. Hence, on one fixed end, we sandwiched the beam between two metal blocks and clamped them together to the table, as shown in Fig. 2(b). Furthermore, to ensure that the system is not statically indeterminate, we had to allow the axial load to be taken by the beam. To have the second end in fixed condition and to avoid indeterminacy, displacement was allowed only in the axial direction, and rotation in all the directions was arrested. So, we sandwiched the beam between metal blocks on rollers instead of clamping them to the table. Due to rollers, the beam was allowed to freely displace in the axial direction of the beam which led the system to be statically determinate and allowed the axial load to be experienced by the beam instead of support. A dead weight was kept on top of sandwiched metal blocks to ensure that it did not lift off the ground during impact load or vibration of the beam. The setup to achieve this boundary condition is shown in Fig. 2(c).
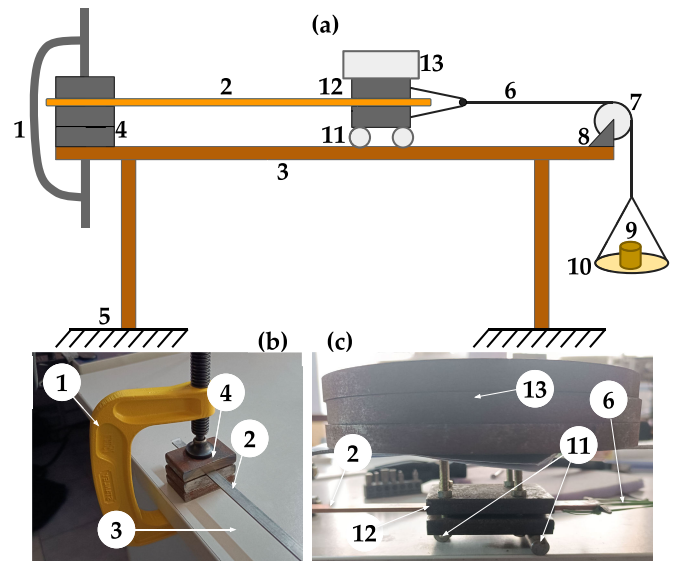


Fig. 2. Fixed-fixed boundary condition implementation. 1—Clamp. 2—Beam. 3—Table. 4—Metal blocks. 5—Ground. 6—Cable. 7—Pulley. 8—Pulley fixture. 9—Weights. 10—Pan. 11—Rollers. 12—Metal blocks. 13—Dead weight. (a) Schematic of the experimental setup. (b) and (c) Photographs showing the mechanisms of the fixed-fixed boundary conditions.

*3) Beam in Fixed-Pinned Condition:* The fixed boundary condition was achieved by sandwiching the beam between two metal blocks and clamping it to the table, similar to the previous cases. To achieve the pinned condition, a pin-housing structure with rollers was prepared. This arrangement restricts the displacement in the transverse direction but allows rotation and displacement in the axial direction of the beam. Instead of clamping the pin-housing structure to the table, four roller bearings were attached to it, two on each side, to make sure that movement in the axial direction was not restricted. Free displacement in the axial direction of the beam made the system to be statically determinate. A dead weight was kept on the pin-housing structure to ensure that it does not lift off the ground during impact load or vibrations of the beam. As the parts used are similar, the schematic of this setup is shown in Fig. S1 of the Supplementary Material.

*4) Beam in Pinned-Pinned Condition:* The schematic of this setup is shown in Fig. 3(a). On one end of the beam, we implemented the pin-housing structure with rollers similar to the fixed-pinned case. On the other end of the beam, the pin-housing structure, discussed for the fixed-pinned case, was implemented without the use of rollers. This pin-housing structure was clamped to the table to restrict displacement in the axial direction of the beam. The photographs showing the implementation of the boundary conditions are shown in Fig. 3(b) and (c).

*5) Application of Load:* Tensile axial loads were applied on all the beams. One end of the beam was attached to a cable. The cable was passed over a fixed pulley, stationed on a fixture. This assembly is held firmly onto a table by the clamp. The photograph showing the arrangement is given in Fig. 4(a). A pan is hung to the cable. Known weights were loaded on the pan. This is shown in Fig. 4(b). For all the experiments, the pan used to place weights weighs 0.42 kg.
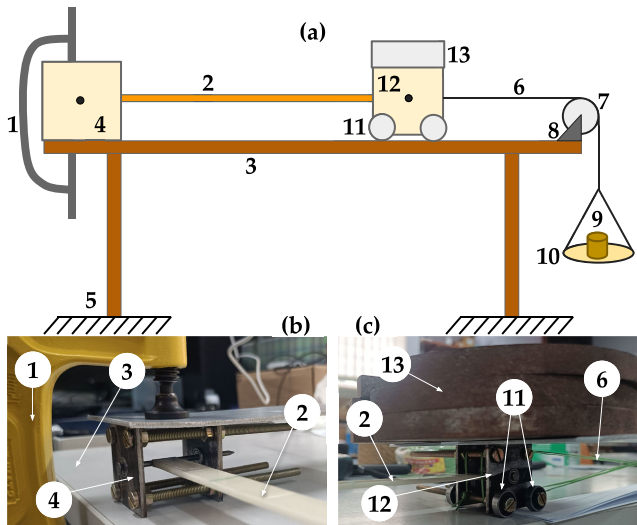
Fig. 3. Pinned-pinned boundary condition implementation. 1—Clamp. 2—Beam. 3—Table. 4—Pin-housing arrangement clamped to table. 5—Ground. 6—Cable. 7—Pulley. 8—Pulley fixture. 9—Weights. 10—Pan. 11—Rollers. 12—Pin housing. 13—Dead weight. (a) Schematic of the experimental setup. (b) and (c) Pinned-pinned boundary condition implementation mechanism.
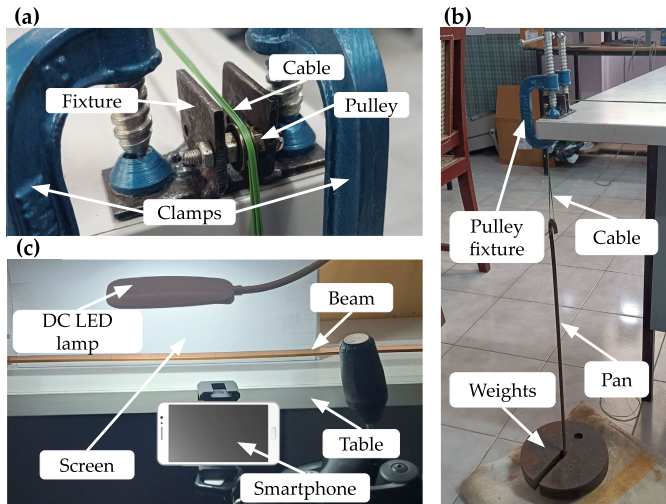


Fig. 4. (a) and (b) Mechanisms comprising clamps, cables, pulleys, and fixtures, used to apply a steady axial load on the beams. (c) Arrangement of lamp, tripod, and screen to record the vibrations of the beam.

### C. Procedure

The following steps were followed in sequence to perform experiments. The specimen was fixed with the required boundary condition, and axial load was applied by placing weights on the pan. The screen and lights were set up properly, and a smartphone (camera) was fixed to the tripod as shown in Fig. 4(c). The camera was placed at ∼ 25 cm from the beam. Slow motion video capture mode with 240 frames/s was turned on in the camera of a smartphone (X7 Max, Realme, China), and a palm-held Bluetooth trigger device (BT-5125, Popio World, India) was connected to the phone. An impact load was given to the specimen with the flick of a finger. A Bluetooth trigger was also attached to the author's finger, which begins to record the video upon the flick by the finger. Simultaneously, the trigger was activated to record the video. The video was

recorded for 4–5 s. The same procedure was adopted for all the experiments, and in the end, all the videos were transferred to a computer for processing. Computer programs, which feed on these videos along with the point of interest (PoI) in each video, were developed to determine the value of the natural frequency, i.e., the frequency of the first mode of vibrations. This natural frequency value was noted. Eight specimens, four different boundary conditions, and ten different axial loads varying from 0.5 to 5 kg were used. A total of 320 experiments were performed. Some experiments were performed on the specimens, with three different lengths, in fixed-free boundary conditions without the axial load, resulting in another 24 experiments. Experiments without axial load were aimed to estimate Young's moduli of the materials.

### III. IMAGE PROCESSING

The optical video of the vibrating beams was processed to detect the natural frequency of beam. A computer program was developed to track the position of chosen points with time. All the programs were written in Python [31] using Jupyter notebook [32].

### A. Algorithm

The point tracking program requires the video and coordinates of the PoI in image pixel coordinates as inputs. The PoI is selected manually by the user. In our workflow, we displayed the first frame (reference frame) of the video in the interactive python notebook (.ipynb) and chose the coordinates that represent the PoI on the beam. A rectangular region was chosen as the search area. All the points that have the same $y$-coordinate were taken as search area (rectangle with width 1-pixel width). This was done as there was almost no horizontal movement for the PoI. If the horizontal axis of the camera/image is not aligned with the beam axis, then we increased the width of the search region from 1-pixel width to any desired value. Once the search region was selected, all the points in it were considered to be potential positions of PoI in the subsequent frames. For example, to exactly determine the current position of the PoI in the second frame, we extracted a square window of width 11 pixels around the PoI in the reference frame (first frame). A similar window around each point in the search space in the second frame was selected, and the SAD was calculated for each window in the second frame. A point in the search space with the least value of SAD was considered to be the current position of the reference point in the second frame. This process was repeated to determine the position of PoI in every frame. As the frame rate is known, the time-dependent displacement of the PoI is extracted. This process along with the next steps is illustrated in Fig. 5.

### B. Point of Interest

Since the algorithm tracks the initially specified reference point (PoI) in the first frame, points were carefully chosen for accurate tracking. The point selected on the beam had sufficient contrast with its local neighborhood such that it can be differentiated from its background. Furthermore, the points had roughly the same background throughout the experiment
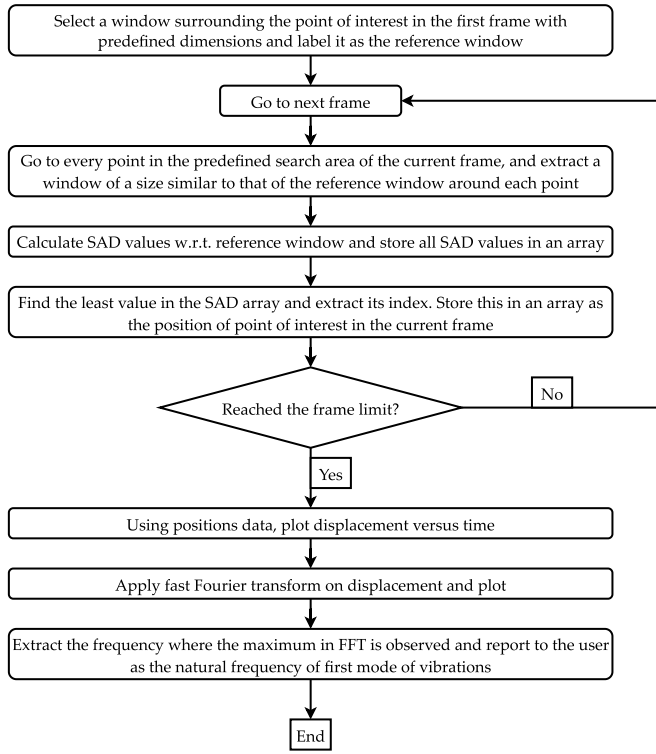
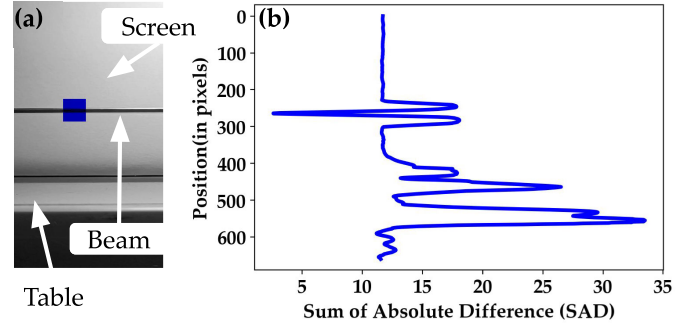Fig. 5. Flowchart of the point tracker algorithm.



Fig. 6. (a) Random frame of the video with parts marked. (b) Estimated position of the PoI from the correlation plot. *Note that the video frame is cropped to a different aspect ratio in this figure for better visualization.

for the program to accurately track its position. This was achieved by placing a white screen behind the beam, as shown in Fig. 4(c).

## IV. THEORY

Euler–Bernoulli's thin beam assumption was used to derive the relationship between natural frequency and axial load. The equation of motion of the axially loaded beam is

$$EI\frac{\partial^4 w(x,t)}{\partial x^4} - P\frac{\partial^2 w(x,t)}{\partial x^2} + \rho A\frac{\partial^2 w(x,t)}{\partial t^2} = 0 \quad (1)$$

where $E$ is Young's modulus, $I$ is the area moment of inertia of the cross section of the beam about the neutral axis, $\rho$ is the mass density, $w$ is the displacement in the flexural direction of the beam, $P$ is the axial load, $x$ is along the axis of the beam, and $t$ is time. We seek the well-established ansatz of the form [33]

$$W(x) = C_1 \sinh(M\zeta) + C_2 \cosh(M\zeta)$$
$$+ C_3 \sin(N\zeta) + C_4 \cos(N\zeta) \quad (2)$$

where $M = (U + (U^2 + \Omega^2)^{1/2})^{1/2}$, $N = (-U + (U^2 + \Omega^2)^{1/2})^{1/2}$, $\zeta = x/L$ is a nondimensional space coordinate in the axial direction of beam, $L$ is the length of the beam, with $U = PL^2/2EI$, $\Omega = \omega L^2/\alpha$, $\alpha = (EI/\rho A)^{1/2}$, and $\{C_1, C_2, C_3, C_4\}$ are arbitrary constants determined based on the boundary conditions. Except for the pinned-pinned case, the other three cases do not have an exact relationship between natural frequency and axial load.

Blevins and Plunkett [34] provided approximate relationships between natural frequency and axial load for other cases.

The approximate dependency of natural frequency $f$ of the first mode on axial load for a fixed-free beam is

$$f = \frac{\lambda_{xe}^2}{2\pi L^2}\sqrt{\frac{EI}{m}}\left(1 + \frac{P}{|P_b|}\right) \quad (3)$$

where $\lambda_{xe} = 1.8751$, $m = \rho A$ is mass per unit length of beam, $P_b = \pi^2 EI/4L^2$ is the critical buckling load of the first mode, and $|\cdot|$ denotes the absolute value of the argument. The approximate relationship between axial load and natural frequency of the first mode for fixed-fixed beam is

$$f = \frac{\lambda_{xx}^2}{2\pi L^2}\sqrt{\frac{EI}{m}}\left(1 + \frac{P}{|P_b|}\right) \quad (4)$$

where $\lambda_{xx} = 4.73$ and $P_b = 4\pi^2 EI/L^2$. For fixed-pinned condition, the approximate relationship between axial load and natural frequency of the first mode becomes

$$f = \frac{\lambda_{xp}^2}{2\pi L^2}\sqrt{\frac{EI}{m}}\left(1 + \frac{P}{|P_b|}\right) \quad (5)$$

where $\lambda_{xp} = 3.9266$ and $P_b = 2.05\pi^2 EI/L^2$. For pinned-pinned condition, we have an exact relationship between axial load and natural frequency of the first mode as

$$f = \frac{\lambda_{pp}^2}{2\pi L^2}\sqrt{\frac{EI}{m}}\left(1 + \frac{P}{|P_b|}\right) \quad (6)$$

where $\lambda_{pp} = \pi$ and $P_b = \pi^2 EI/L^2$.

## V. RESULTS AND DISCUSSION

### A. Demonstration of Algorithm

A random frame from the video of a specimen is shown in Fig. 6(a). Here, the area highlighted in blue represents the window around the tracked point. The correlation plot for the frame is shown in Fig. 6(b). The $Y$-axis represents the vertical coordinate of the points in the search area and the $X$-axis represents the SAD value. We note that the value of SAD is minimum wherever the beam is present.

### B. Estimation of Young's Modulus

Each specimen was kept in fixed-free boundary condition and length was varied to determine Young's modulus $E$. The variation in length was achieved using the nonmoving fixed

TABLE II

ESTIMATED YOUNG'S MODULUS $E$ OF SPECIMENS OBTAINED FROM
BEAMS, WITH NO AXIAL LOAD, UNDER FIXED-FREE
BOUNDARY CONDITION

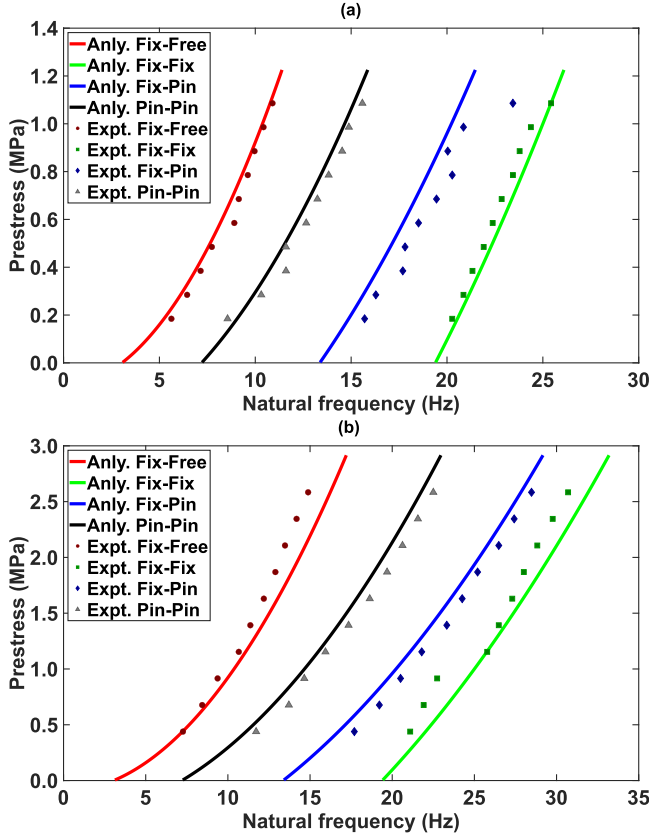| Specimen ID | Average $E$ (GPa) | Specimen ID | Average $E$ (GPa) |
|---|---|---|---|
| 1 | 58.58 | 5 | 113.70 |
| 2 | 58.58 | 6 | 123.70 |
| 3 | 172.61 | 7 | 16.77 |
| 4 | 166.87 | 8 | 16.77 |



Fig. 7. Comparison of analytically and experimentally identified natural frequencies with different levels of loads for aluminum specimens of (a) ID 1 and (b) ID 2. Anly. and Expt. stand for analytical and experimental values, respectively.
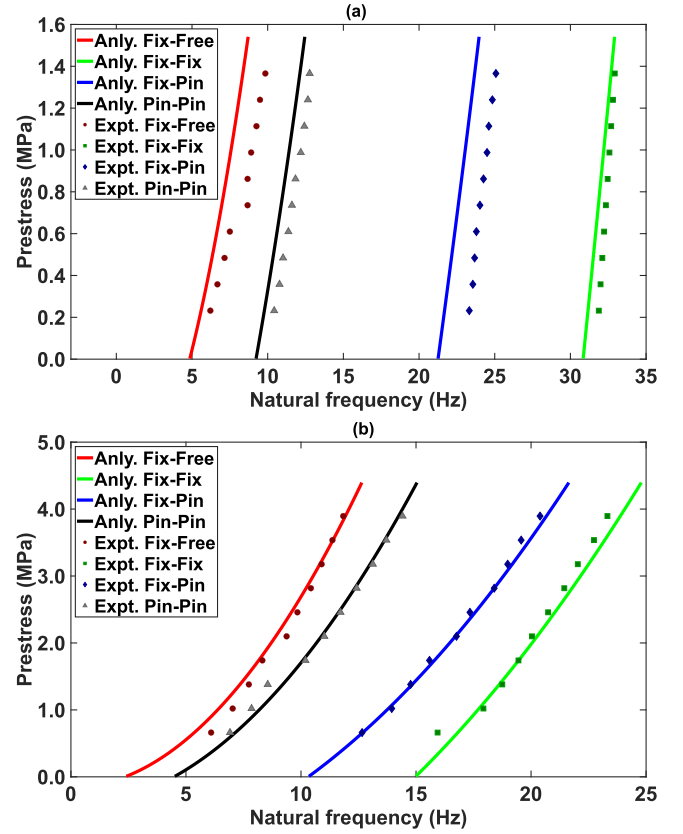


Fig. 8. Comparison of analytically and experimentally identified natural frequencies with different levels of loads for steel specimens of (a) ID 3 and (b) ID 4. Anly. and Expt. stand for analytical and experimental values, respectively.

boundary condition mechanism at different positions on the beam. The displacement at a PoI was estimated as a function of time. The fast Fourier transform was used on these data to estimate the spectral regime of the vibration and natural frequency. Next, $E$ was calculated as [34]

$$f = \frac{\lambda^2}{2\pi L^2}\sqrt{\frac{EI}{m}} \qquad (7)$$

where $\lambda = 1.8751$ and $m$ is the mass per unit length of beam. The results of the calculated average Young's moduli are shown in Table II. These were used for the estimation of prestress.

### C. Estimation of Prestress

Following the procedure detailed in Sections III and IV, we first estimated Young's modulus. Then, the natural frequencies $f$ were determined for all the specimens in all

four boundary conditions. Based on the estimated $f$, using (3)–(6), we estimated the preload $P$ and the prestress on the beams. Since the estimated prestress is based on theory and image processing, we refer to the former as an analytical value and the applied prestress as an experimental value. The comparisons of the analytically and experimentally estimated prestresses with different axial loads (natural frequencies) for aluminum specimens, corresponding to IDs 1 and 2, for different boundary conditions are shown in Fig. 7(a) and (b), respectively. We make the following conclusions.

1) A good correlation was observed for the estimated and experimental values of prestress, regardless of the applied load and the boundary conditions of the specimen. This indicates that the longitudinal prestress in beams can be estimated using simple CV experiments based on smartphone camera and programs.

2) As expected, the specimen with the fixed-free boundary conditions has the largest resonant wavelength (four times the length of the beam), leading to the lowest natural frequency. Furthermore, the beams under fixed-fixed boundary conditions have the least possible wavelength (equal to the length of the beam), leading to the highest resonant frequency for a given load.

3) Minor differences in the experimental and analytical natural frequencies were found. The reasons for this are two-fold: a) the expressions used for the analytical calculations are a good approximation and not an exact
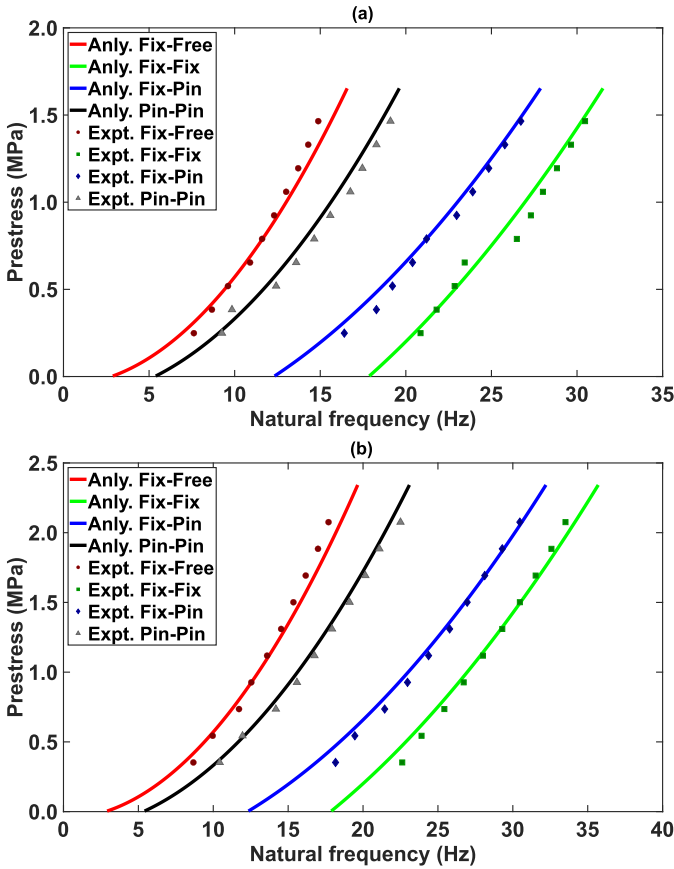
Fig. 9. Comparison of analytically and experimentally identified natural frequencies with different levels of loads for GFEC specimens of (a) ID 7 and (b) ID 8. Anly. and Expt. stand for analytical and experimental values, respectively.

is reliable. We further note that for all the specimens, the highest deviation is observed for those specimens with a free boundary condition. This is expected due to the larger degrees of freedom associated with this boundary condition.

### D. Error Analysis

We have performed a detailed error analysis, as shown in the Supplementary Material. We found that statistically, the error in estimating the value of prestress is less than 10% in at least 93% of the experiments. The low value is in line with the results shown for all the specimens, where a close match is observed between the experimentally and theoretically estimated prestresses. We found that a large component contributing to the error in prestress is the error from estimation of Young's modulus. This indicates that the error can be minimized if Young's modulus is known. The results shown in Figs. 7–9 indicate that in our experiments, the actual error, which is the difference in analytical and estimated values, is far less than 5% in many cases at multiple loads or frequencies. Both the error analysis and the results indicate that our experiments are reliable and that the simple setup developed is robust.

## VI. Conclusion

In this work, using a combination of image processing and theory, we estimated the prestresses in beams of various lengths, made of different materials, and subjected to various boundary conditions. Toward this, four experimental setups were built. Prestress was estimated by correlating the analytical and experimentally identified natural frequencies. The novelty of our work lies in using simple CV methods to estimate the prestress in beams. The main advancement of this work is the demonstration of proof of concept to measure prestress using noncontact nondestructive methods. Based on the goodness of the results, we plan to extend this work in three ways. First, these experiments can be extended to lateral loads on the beams with modifications in the equipment. Second, machine vision methods can be developed to estimate Young's modulus and prestress in beams simultaneously. Third, the experiments can be performed on 3-D objects in tandem with finite element simulations to determine the prestresses.

## Authors' Contributions

The project was conceived by C. Chandraprakash. B. Yaswanth Sandeep performed all the experiments and computations. B. Yaswanth Sandeep and C. Chandraprakash did the writing.

## Data Sharing

The data and code supporting the findings of this study are available from the authors upon reasonable request.

## Acknowledgment

The authors are thankful to Shri Ramchand Tiwari, Mechanical Engineering, IIT Kanpur, for his help in fabricating the composite beam. They are also thankful to Shri Anil Jha and the Central Workshop staff for their assistance in experiments.

value and b) as the load increases, the approximations of the Euler–Bernouli beam theory for the flexure of specimens are gradually evaded.

Furthermore, some experimental errors could be due to: 1) pins on the edges of beams, used to implement pin conditions, are not considered in the analytical model; 2) internal damping and air resistance were not considered in the analytical model; 3) due to vibrations, the angle of application of load might change in fixed-free case; and 4) the camera has a limit on maximum frame rate and hence a limit exists on the resolution of frequency space. In our case, it is 0.6 Hz.

The comparison of the analytically estimated and experimentally estimated prestresses with different axial loads (natural frequencies) for stainless steel specimens, IDs 3 and 4, for different boundary conditions are shown in Fig. 8(a) and (b), respectively. Similar plots for the copper specimens, IDs 5 and 6, for different boundary conditions are shown in Fig. S2(a) and (b), respectively, in the Supplementary Material. Likewise, the plots for glass fiber epoxy composites (GFECs), IDs 7 and 8, for different boundary conditions are shown in Fig. 9(a) and (b), respectively. The conclusions from the results of the stainless steel, copper, and GFECs remain the same as those from the results of aluminum specimens. With the good correlations between experimentally imposed prestress and the estimated value using analytical work for various materials, we conclude that the technique developed

## REFERENCES

[1] M. Saatcioglu and C. Yalcin, "External prestressing concrete columns for improved seismic shear resistance," *J. Structural Eng.*, vol. 129, no. 8, pp. 1057–1070, Aug. 2003, doi: 10.1061/(asce)0733-9445(2003)129:8(1057).

[2] R. El-Hacha, "Prestressing concrete structures with FRP tendons (ACI 440.4R-04)," in *Proc. Struct. Congr.*, Apr. 2005, pp. 1–8, doi: 10.1061/40753(171)160.

[3] B. Tveiten, A. Fjeldstad, G. Harkegard, O. Myhr, and B. Bjorneklett, "Fatigue life enhancement of aluminium joints through mechanical and thermal prestressing," *Int. J. Fatigue*, vol. 28, no. 12, pp. 1667–1676, Dec. 2006, doi: 10.1016/j.ijfatigue.2006.01.006.

[4] S.-K. Hong, B. I. Epureanu, and M. P. Castanier, "Parametric reduced-order models of battery pack vibration including structural variation and prestress effects," *J. Power Sources*, vol. 261, pp. 101–111, Sep. 2014, doi: 10.1016/j.jpowsour.2014.03.008.

[5] H. N. Garden and L. C. Hollaway, "An experimental study of the failure modes of reinforced concrete beams strengthened with prestressed carbon composite plates," *Compos. B, Eng.*, vol. 29, no. 4, pp. 411–424, Jan. 1998, doi: 10.1016/s1359-8368(97)00043-7.

[6] M. Moravcik, P. Bujnakova, and F. Bahleda, "Failure and damage of a first-generation precast prestressed bridge in Slovakia," *Structural Concrete*, vol. 21, no. 6, pp. 2353–2362, Dec. 2020, doi: 10.1002/suco.201900526.

[7] F. D. Murnaghan, "The compressibility of media under extreme pressures," *Proc. Nat. Acad. Sci. USA*, vol. 30, no. 9, pp. 244–247, Sep. 1944, doi: 10.1073/pnas.30.9.244.

[8] J.-F. Chai and T.-T. Wu, "Determination of surface wave velocities in a prestressed anisotropic solid," *NDT E Int.*, vol. 29, no. 5, pp. 281–292, Oct. 1996, doi: 10.1016/s0963-8695(96)00031-x.

[9] M. Miniaci, M. Mazzotti, A. Amendola, and F. Fraternali, "Effect of prestress on phononic band gaps induced by inertial amplification," *Int. J. Solids Struct.*, vol. 216, pp. 156–166, May 2021, doi: 10.1016/j.ijsolstr.2020.12.011.

[10] W.-H. Hu, S. Said, R. G. Rohrmann, Á. Cunha, and J. Teng, "Continuous dynamic monitoring of a prestressed concrete bridge based on strain, inclination and crack measurements over a 14-year span," *Structural Health Monitor.*, vol. 17, no. 5, pp. 1073–1094, Sep. 2018, doi: 10.1177/1475921717735505.

[11] H. Aben, J. Anton, and A. Errapart, "Modern photoelasticity for residual stress measurement in glass," *Strain*, vol. 44, no. 1, pp. 40–48, Feb. 2008, doi: 10.1111/j.1475-1305.2008.00422.x.

[12] B. Dubuc, A. Ebrahimkhanlou, and S. Salamone, "Stress monitoring of prestressing strands in corrosive environments using modulated higher-order guided ultrasonic waves," *Structural Health Monitor.*, vol. 19, no. 1, pp. 202–214, Jan. 2020, doi: 10.1177/1475921719842385.

[13] F. Morelli et al., "Assessment of the residual prestressing force in existing bridges through the X-ray diffractometer," in *Proc. Int. Conf. Eur. Association Quality Control Bridges Struct.* Cham, Switzerland: Springer, 2021, pp. 870–876, doi: 10.1007/978-3-030-91877-4_99.

[14] A. Azizinamini, B. J. Keeler, J. Rohde, and A. B. Mehrabi, "Application of a new nondestructive evaluation technique to a 25-year-old prestressed concrete girder," *PCI J.*, vol. 41, no. 3, pp. 82–95, May 1996, doi: 10.15554/pcij.05011996.82.95.

[15] J. Chen, X. Wan, and Q. Guo, "Monitoring of stress variation of strands in prestressed concrete by second harmonic generation measurements based on piezoelectric sensors," *Smart Mater. Struct.*, vol. 31, no. 1, Nov. 2021, Art. no. 015004, doi: 10.1088/1361-665x/ac36e1.

[16] P. Lundqvist and N. Rydén, "Acoustoelastic effects on the resonance frequencies of prestressed concrete beams—Short-term measurements," *NDT E Int.*, vol. 50, pp. 36–41, Sep. 2012, doi: 10.1016/j.ndteint.2012.04.010.

[17] B. Zhong, J. Zhu, and G. Morcous. (2020). *Development of an NDT Tool for In-Situ Assessment of Prestress Loss*. [Online]. Available: https://digitalcommons.unl.edu/ndor/244/

[18] L. Scime and J. Beuth, "Anomaly detection and classification in a laser powder bed additive manufacturing process using a trained computer vision algorithm," *Additive Manuf.*, vol. 19, pp. 114–126, Jan. 2018, doi: 10.1016/j.addma.2017.11.009.

[19] T. H. Dinh et al., "Toward vision-based concrete crack detection: Automatic simulation of real-world cracks," *IEEE Trans. Instrum. Meas.*, vol. 72, pp. 1–15, 2023.

[20] A. Kumar and C. Chandraprakash, "Estimation of planar angles from non-orthogonal imaging," *Rev. Sci. Instrum.*, vol. 95, no. 1, pp. 1–8, Jan. 2024, doi: 10.1063/5.0173906.

[21] (2023). *The 87 Most Popular Computer Vision Applications for 2023*. [Online]. Available: https://viso.ai/applications/computer-vision-applications/

[22] H. Zhang et al., "Automated machine vision system for liquid particle inspection of pharmaceutical injection," *IEEE Trans. Instrum. Meas.*, vol. 67, no. 6, pp. 1278–1297, Jun. 2018.

[23] Q. Luo, X. Fang, L. Liu, C. Yang, and Y. Sun, "Automated visual defect detection for flat steel surface: A survey," *IEEE Trans. Instrum. Meas.*, vol. 69, no. 3, pp. 626–644, Mar. 2020.

[24] A. Kumar and C. Chandraprakash, "Computer vision-based on-site estimation of contact angle from 3-D reconstruction of droplets," *IEEE Trans. Instrum. Meas.*, vol. 72, pp. 1–8, 2023, doi: 10.1109/tim.2023.3291797.

[25] A. Davis* et al., "Visual vibrometry: Estimating material properties from small motions in video," *IEEE Trans. Pattern Anal. Mach. Intell.*, vol. 39, no. 4, pp. 732–745, Apr. 2017, doi: 10.1109/TPAMI.2016.2622271. https://doi.org/10.1109/CVPR.2015.7299171

[26] D. J. Fleet and A. D. Jepson, "Computation of component image velocity from local phase information," *Int. J. Comput. Vis.*, vol. 5, no. 1, pp. 77–104, Aug. 1990, doi: 10.1007/bf00056772.

[27] W. T. Freeman and E. H. Adelson, "The design and use of steerable filters," *IEEE Trans. Pattern Anal. Mach. Intell.*, vol. 13, no. 9, pp. 891–906, Sep. 1991. [Online]. Available: http://people.csail.mit.edu/billf/www/papers/steerpaper91FreemanAdelson.pdf

[28] M. A. Shabani, L. Samadfam, and M. A. Sadeghi, "Local visual microphones: Improved sound extraction from silent video," 2018, *arXiv:1801.09436*.

[29] B. K. P. Horn and B. G. Schunck, "Determining optical flow," *Artif. Intell.*, vol. 17, nos. 1–3, pp. 185–203, Aug. 1981.

[30] N. McCormick and J. Lord, "Digital image correlation," *Mater. Today*, vol. 13, no. 12, pp. 52–54, Dec. 2010, doi: 10.1016/s1369-7021(10)70235-2.

[31] M. Pilgrim and S. Willison, *Dive Into Python 3*, vol. 2. Berkeley, CA, USA: Springer, 2009, doi: 10.1007/978-1-4302-2416-7.

[32] T. Kluyver et al., "Jupyter notebooks—A publishing format for reproducible computational workflows," in *Positioning and Power in Academic Publishing: Players, Agents and Agendas*, F. Loizides and B. Schmidt, Eds., Amsterdam, The Netherlands: IOS Press, 2016, pp. 87–90.

[33] A. Bokaian, "Natural frequencies of beams under tensile axial loads," *J. Sound Vibrat.*, vol. 142, no. 3, pp. 481–498, Nov. 1990, doi: 10.1016/0022-460x(90)90663-k.

[34] R. D. Blevins and R. Plunkett, "Formulas for natural frequency and mode shape," *J. Appl. Mech.*, vol. 47, no. 2, pp. 461–462, Jun. 1980, doi: 10.1115/1.3153712.

**B. Yaswanth Sandeep** received the B.Tech. degree in mechanical engineering from IIT Patna, Patna, India, in 2019, and the M.Tech. degree in mechanical engineering from IIT Kanpur, Kanpur, India, in 2022.

He is currently a Data Scientist with Decimal Point Analytics, Mumbai, India. His current work includes utilization of machine learning and deep learning to solve problems in traffic forecasting and predictive maintenance.

**C. Chandraprakash** received the B.Tech. and M.Tech. degrees in mechanical engineering from IIT Madras, Chennai, India, in 2010, and the Ph.D. degree in engineering science and mechanics from The Pennsylvania State University, University Park, PA, USA, in 2017.

He was an Engineer with Tata Motors Ltd., Pune, India, for one year. He is currently an Assistant Professor in mechanical engineering with IIT Kanpur, Kanpur, India. His current research interests include computer vision, multifunctional materials, acoustic metamaterials, thermal and ultrasonic nondestructive evaluation, and biomimicry.